Tumor Hypoxia and Blood Vessel Detection

An Image Analysis Technique for Simultaneous Tumor Hypoxia Grading and Blood Vessel Detection in Tissue Sections

CONSTANTINOS G. LOUKAS,[a,b] GEORGE D. WILSON,[a]
BORIVOJ VOJNOVIC,[a] AND ALF LINNEY[b]

[a]*Gray Cancer Institute, Mount Vernon Hospital, Northwood, Middlesex, United Kingdom*

[b]*Department of Medical Physics and Bioengineering,*
University College London, Shropshire House, London, United Kingdom

ABSTRACT: We have developed a multistage image analysis technique for the simultaneous segmentation of blood vessels and hypoxic regions in dual-stained tumor tissue sections. The algorithm, which is integrated in a task-oriented image analysis system developed on-site, initially uses the *K*-nearest neighbor classification rule in order to label the image pixels. Classification is based on a training set selected from manually drawn regions corresponding to the areas of interest. If the output image contains a significant number of misclassified pixels, the user has the option to apply a series of specific problem-designed routines (texture analysis, fuzzy *c*-means clustering, and edge detection) in order to improve the final segmentation result. Validation experiments indicate that the algorithm can robustly detect these biological features, even in tissue sections with a very low quality of staining. This approach has also been combined with other image analysis based procedures in order to objectively obtain quantitative measurements of potential clinical interest.

KEYWORDS: image analysis; hypoxia; vasculature; classification; blood vessel segmentation

INTRODUCTION

Hypoxia and tumor vasculature are two biological features that play a crucial role in the radiation response of solid tumors. Both the importance of tumor oxygenation and the relevance of blood flow, for the outcome of radiation treatment, were described many years ago by Schwartz,[1] and Gray *et al.*,[2] respectively. Solid tumors represent 90% of all human cancer and are characterized by much lower oxygenation levels than normal tissues, leading to increased resistance to radiotherapy and anti-cancer chemotherapy, as well as a predisposition to increased tumor metastases.[3] The growth of a solid tumor requires the induction of its own blood supply, which it does by stimulating the growth of cells from surrounding vessels into the tumor, a

Address for corresponding: C. Loukas, Sobell Department of Motor Neuroscience and Movement Disorders, Institute of Neurology, Queen Square, London WC1N 3BG, UK. Voice: +44 0 207 837 3611, ext. 4319; fax: +44 0 207 278 9836.
c.loukas@ion.ucl.ac.uk

Ann. N.Y. Acad. Sci. **980: 125–138 (2002).**

process that is referred to as *angiogenesis*. However, the newly formed vascular network in the tumor is very chaotic and as a result, blood flow is highly irregular, causing the development of nutritient- and oxygen-deprived regions. This leads to the development of both chronic (diffusion-limited) and acute (perfusion-limited) hypoxia.

There is much current interest in the clinical significance of these different forms of hypoxia yet the *gold standard* method for assessing hypoxia uses an Eppendorf microelectrode. This method measures tissue oxygenation in the region of the electrode tip and cannot provide any information pertaining to the different forms of hypoxia. Very few of the current methods are easily accessible in routine clinical practice, and correlations with the outcome of radiotherapy are still few.[4] In addition, even those studies attempting to investigate the relationship between the tumor vascular architecture and oxygenation, suffered from major pitfalls as they failed to extract subcellular scale information, or lacked the implementation of formal validation studies.

Image analysis has yet to contribute significantly to the investigation of hypoxia and tumor vasculature, and most of the algorithmic approaches to date have focussed on imaging modalities of limited resolution and with poor spatial information.[5,6] For example, Charpin *et al.*[7] and Strieth *et al.*[8] used image analysis to evaluate tumor angiogenesis in tissue sections that contained CD31 immunostained blood vessels, providing, however, very limited information on how the blood vessel detection is achieved. Haustermans *et al.* described a technique within existing image analysis software that allows an estimation of the presence of hypoxia in a tumor, based on vascular parameters.[9] According to that study, hypoxic areas as well as blood vessels were detected by thresholding, and staining artifacts were removed by manual interaction. The proportion of tumor tissue area greater than a fixed distance from the nearest stained blood vessel was subsequently calculated. Rijken and coworkers developed more advanced techniques,[10–12] but the processing is performed on tissue section images acquired by means of fluorescence microscopy, where features of interest are much more easily distinguishable. None of the previously mentioned studies have reported validation experiments, which would exhibit the reliability of the proposed techniques, or provided details concerning the image analysis algorithms. Rather, they concentrate on clinical conclusions.

Following the previous discussion, there is a great need to standardize the methods of quantification and extract as much useful information as possible from immunohistochemically stained tissue sections. The aim of this study was to develop a novel image analysis technique for studying tumor hypoxia in relation to the functional vascular geometry with direct quantitative measurements within different tumor regions. Specifically, we used a multistage algorithm that focuses on simultaneous grading and detection of hypoxic regions and blood vessels, respectively, present in large-scale histological images, acquired by means of light microscopy. The following sections describe the analyzed histologic material and the algorithmic steps of the method proposed. Quantitative results are provided in the form of correct pixel labeling and image classification of tumor samples encountered in clinical practice.

MATERIALS

The specimens studied were histologic sections from various human bladder cell carcinomas that had been doubled stained using standard immunohistochemistry for hypoxia and vasculature. Blood vessels were identified with a monoclonal antibody against CD31, which is expressed on the surface of endothelial cells. Visualization of the antibody complex was achieved with a chemical reaction using diaminobenzidine, resulting in brown staining of the endothelial cell membranes. To stain hypoxic cells, patients were injected with pimonidazole hydrochloride 16–24 hours prior to surgery. This is a bioreductive agent that is only fully metabolized and binds in the absence of oxygen. Binding was recognized by a monoclonal antibody and visualized using vector red through an alkaline phosphatase reaction. All nuclei in the sections were counterstained blue using haematoxylin.

The tissue-section images were captured as three-color 768×576 bitmaps using a Zeiss Axioscop trans-illumination microscope, coupled to a JVC KY55F 1/3″ (6.4×4.8 mm) 3-CCD color camera. Images were digitized using a Matrox Meteor™ frame grabber, installed in a PCI bus 600 MHz Pentium™ PC. A ×40 oil-immersion lens (NA = 0.75) was used during acquisition, providing a compromise between adequate resolution and maximum field of view of the region of interest. The pixel size, using a ×0.5 demagnifier before the camera, at the object plane ($241.5 \times 180.5\,\mu\text{m}$) was $0.3\,\mu\text{m} \times 0.3\,\mu\text{m}$. Each point in the image corresponded to a point in a three-dimensional (3D) vector space, with each location in the scene consisting of R (red), G (green), and B (blue) components.

IMAGE ANALYSIS

This section describes the multistage technique for simultaneous segmentation and grading of blood vessels and hypoxia, respectively. After the image is captured with the hardware set-up described above, the user can perform various measurements with an image analysis system that includes task-oriented operations. The individual steps involved in the processing of the tissue section images are shown in FIGURE 1.

Training Set

As stated in the introduction, the processing is initiated with the user prompted to manually draw polygons, corresponding to the various features being segmented on the displayed histologic image: the histologic background containing tumor cells (BG), blood vessels (BV), high level hypoxic regions (HH), and low level hypoxic regions (LH), which exhibit the same color as HH but are significantly weaker, due to smaller uptake of the hypoxia marker. The resulting quantitative data constituted a training set (i.e., data set), characterized by the *red*, *green*, and *blue* color features, which was different for each of the 15 histologic images used in this study. To test if additional or different color features produce better segmentation results, three other spaces were also defined: (1) The RGBMrMgMb space, which is defined by the R, G, and B values, plus the average intensities of the 3×3 nearest neighborhood around

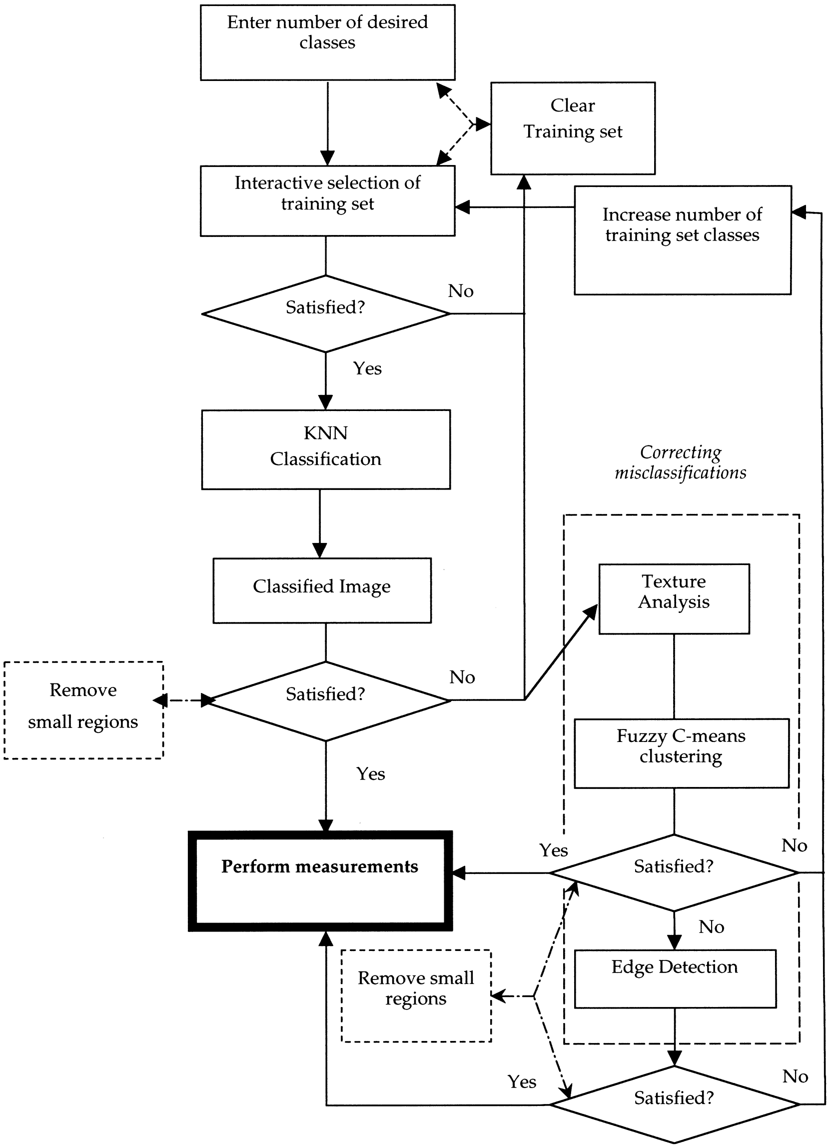

FIGURE 1. Flow-chart of the proposed multistage algorithm.

an image pixel; and (2) The La*b* and Lu*v* color models, which represent color and intensity independently, and are used regularly for color segmentation tasks.[13]

KNN Classifier

After the training set is selected, the user can either delete it and redraw different regions, or proceed to the pixel labeling stage. The algorithm uses a K-nearest-neighbor (KNN) classifier to label all the remaining points of the histologic image. This is essentially a non-parametric classification procedure that can be used without assuming that the forms of the underlying densities, which can be extracted from the training set, are known. Let ω_i, $i = 1, \ldots, 4$ represent the four pattern classes (i.e., BG, BV, HH, and LH). Suppose the data set contains N_i points in class ω_i and N points in total. Then a sphere (hypersphere if the data set is i-dimensional, where $i > 3$), around the point x is drawn that includes K points irrespective of their class label. Thus, if the volume of this sphere is V and contains K_i points from class i, the class conditional probability, denoted by $p(x/\omega_i)$, has the form $p(x/\omega_i) = K_i/(N_i V)$, and using the Bayes' theorem in accordance with an estimation of the unconditional density $p(x) = K/(NV)$ and prior probability $p(\omega_i) = K_i/N$, the *a posteriori* probability is $P(C_i/x) = K_i/K$, which is merely the fraction of the samples within the sphere that are labeled ω_i. For minimum error rate, the class most frequently represented within the cell is selected (*KNN classification rule*[14]). Thus, in the case where either of the 3D color spaces are used (i.e., RGB, La*b*, or Lu*v*), the classification procedure involves finding a sphere around each image pixel x that contains K points (independent of their class), and then assigning x to the class having the largest number of representatives inside the sphere. Similarly, a hypersphere is fitted in the case where every pixel both in the image and the data set is characterized by the six-dimensional vector: $x_i = (R_i, G_i, B_i, Mr_i, Mg_i, Mb_i)$.

Selecting the Optimum Number of NN

One of the problems encountered frequently in non-parametric methods of density estimation concerns the choice of the constraint (the number of NN in our case) that allows the form of the density to be determined entirely by the data. Specifically, if the value of K is large the procedure becomes more robust, but some of the true structure in the density is smoothed out. Yet K must be much smaller than the minimum of N_i, the number of samples in class ω_i, otherwise the neighborhood is no longer the local neighborhood of the sample. In order to find a compromise for the K value, the *leave-one-out* procedure[15] was used to classify every sample in the RGB training set using the remaining samples, for various values of K. This method was performed for each training set selected from the 15 histological images, and the classifier performance was then averaged producing the curve shown in FIGURE 2. The classifier was tested for each of the first 50 NN, presenting the least misclassifications when $K = 31$, which was used as the optimum K value for labeling the tissue section images. It can be also noticed from the graph that the KNN method performs worse when either a smaller or a larger number of NN are taken into account during the data set classification.

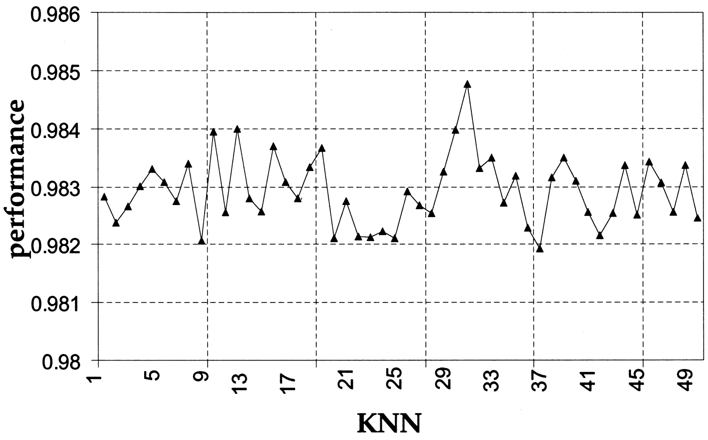

FIGURE 2. Classifier performance versus number of nearest neighbors (NN).

Correcting Misclassifications

After pixel labeling of the tissue section images is complete, the user selects the class of interest (i.e., BV, LH, etc.) and might either proceed to the quantitative analysis menu, if satisfied with the displayed output image, or perform other operations to correct any misclassifications produced, which are usually distributed as small clusters. In the latter instance, the user is provided with the option to apply reversibly a *remove_small_regions* routine (see FIG. 1) that produces a low pass filtered image. However, occasionally during the immunohistochemical staining procedure, some small background regions tend to uptake mistakenly the vessel stain, causing the KNN classifier to produce major misclassifications, since different structures (i.e., BV and BG or LH) retain similar color properties. If so, the user has the option to use problem-specific operations to reclassify those pixels that have been mistakenly labeled BV although they belong to the BG (and rarely to the LH) class. Specifically, if the misclassified pixels form unwanted large regions that cannot be removed without also removing the correctly classified vessels, a sequence of two image analysis techniques combined with a clustering algorithm have been created to further classify the BV class.

Texture Analysis. Prompted by the algorithm proposed by Dubuisson-Jolly and Gupta for color and texture fusion,[16] we used simultaneous autoregressive (SAR) models to compute texture features for each pixel in the R, G, and B plane separately. Specifically, the SAR model defines the grey-level $g(x,y)$ at a pixel location (x,y) as

$$g(x, y) = \mu + \sum_{(i, j) \in N} \theta_{(i, j)} g(x+i, y+j) + \sqrt{\rho_N}\varepsilon(x, y), \tag{1}$$

where N is a neighbor set defined in the spatial domain, $\varepsilon(x)$ is an independent Gaussian random variable with zero mean and unit variance, ρ_N is the overall variance of noise, μ is a sample mean of image grey level values, and $\theta_{(i,j)}$ $((i,j) \in N)$ are the model parameters. Different textures are characterized by different neighborhood properties that, in turn, get represented by different model parameters. There are five texture parameters computed at each pixel and in each color band (i.e., 15 color-texture features overall), using the least squares error technique in a 11×11 window centred on that pixel. Four of them are the direction sensitive parameters $\theta_{(i,j)}$ that capture textural characteristics in the horizontal, vertical, diagonal, and off-diagonal directions, and the other is the overall variance ρ_N of the noise in N, which is a measure of randomness of texture.

Fuzzy c*-Means Clustering.* After the texture features are extracted for each color plane, only those belonging to the pixels enclosed in the BV class are considered for further processing. *The fuzzy c-means clustering*[17] (FCM) algorithm, is used to cluster these pixels into two more subclasses: *true* and *non-true* BV pixels. The clustering begins by selecting the desired cluster number, and randomly initializing C cluster centres. FCM, different from hard clustering, does not make a clear-cut classification of the pixels in the data set. Instead, it creates a fuzzy membership matrix U_{ij} in which each element describes the probability that the jth input vector, x_j, which is first normalized, belongs to the ith cluster center, u_i. Provided that $C = 2$, the following two recurrent equations were used:

$$U_{ij}^{-1} = \sum_{k=1}^{2} \left(\frac{\|x_j - u_i\|^2}{\|x_j - u_k\|^2} \right)^{\frac{1}{m-1}} \tag{2}$$

$$u_i = \frac{\sum_{j=1}^{n} (U_{ij})^m \cdot x_j}{\sum_{j=1}^{n} (U_{ij})^m}, \tag{3}$$

where U_{ij} is the fuzzy membership of x_j to class i and m is the fuzzy factor that determines the degree of fuzziness of the membership function. After finding the membership matrix, each cluster is updated according to all input vectors and the membership between them. This procedure iterates until the membership function converges and then each input vector is assigned to the cluster with the highest probability.

Edge Detection. After applying FCM clustering, both classes are displayed with different color so that the user is able to select the class that contains the *true* BV pixels. However, there is a possibility that the output image might contain falsely some pixels (or pixel clusters), in the *non-true* BV class, although they are part of a blood vessel. If this is the case, the user has the option to apply an edge detection algorithm, which we already proposed in a previous study,[18] in order to detect the boundaries of the blood vessels, and then the entire section can be reconstructed easily from even a tiny, but correctly classified, region within the same vessel section (i.e., *true* BV class), using a standard seed fill algorithm that visits all the pixels enclosed by the detected boundary.

At this point it should be also noticed that if the user is not satisfied with the output image either after FCM clustering or edge detection, the number of training set classes can be increased (see FIG. 1), so that the new added class would correspond to the background regions that possess falsely a color similar to that of blood vessels. That case, however, is not encountered frequently and it happens only when the histologic staining is of very low quality. However, by adding one more class that represents the erroneous uptake of the vessel stain from some background regions, the number of misclassifications can be eliminated (more details are given below).

RESULTS AND DISCUSSION

The image processing software was written in the C^{++} programming language under MS Windows™ 2000. For 768×576 size image data, the overall pixel labeling took 15 min whereas texture analysis, FCM clustering and edge detection required less than 4 min processing for those images that contained significant number of mis-

TABLE 1. Analysis of pixel misclassifications (KNN method)

	Predicted Group Membership				
Actual Group	BG	BV	HH	LH	% Correct
(a) RGB space					
BG	47,398	2,295	0	361	95
BV	4,760	21,894	305	2,014	76
HH	13	214	20,987	419	97
LH	493	1,168	126	18,473	91
Total					90
(b) RGBMrMgMb space					
BG	48,164	1,121	0	769	96
BV	6,302	17,826	236	4,610	62
HH	28	716	17,829	3,058	82
LH	1,203	750	97	18,209	90
Total					84
(c) La*b* space					
BG	42,622	2,386	0	5,046	85
BV	1,765	10,161	7,370	9,677	35
HH	0	0	21,594	38	99
LH	6	13	11,075	9,166	45
Total					69
(d) Lu*v* space					
BG	45,404	2,961	0	1,689	91
BV	4,735	8,823	5,583	9,831	30
HH	6	264	21,113	248	98
LH	389	292	4,380	15,198	75
Total					75

classifications. A test set of various areas corresponding to the four different patterns under investigation (BG, LH, HH, and BV) was selected on full histologic images and submitted to the KNN classifier with a view to quantitatively validating its performance in terms of identification of the biological structures of interest. TABLE 1 shows the confusion matrix analysis (expressed in numbers of pixels), for the RGB, RGBMrMgMb, La*b*, and Lu*v* spaces. The rows of the matrix represent the true pixel classes, whereas the columns represent the chosen classes. Correctly classified pixels appear as entries on the diagonal of the matrix. Although these results confirm the high performance of the KNN classifier when features from the RGB space were used, some confusion can be clearly seen between the BV and LH or BG class, and vice versa. This is mostly due to the fact that some images were acquired from tissue sections containing BG and hypoxic regions that had uptaken falsely the vessel stain, which is a recurring phenomenon during the immunohistochemical staining procedure. We also attempted to test the HSI (hue, saturation and intensity) space, but the nonlinearity computation of the hue component made it impractical, producing severe misclassifications (results are not shown here).

FIGURE 3A illustrates a histologic image containing the biological patterns of interest (in the original color image hypoxic regions appear in red and blood vessels in brown). There are four hypoxic regions (three of them touching the bottom border of the image and the other one at the upper-right corner), and four blood vessels (that at the upper-left corner is essentially a cluster of sections belonging to the same blood vessel). The staining quality in this tissue section is good but it is difficult to identify with confidence the LH and HH regions due to the variation in the red stain. Both the LH and HH regions are part of the same hypoxic area in a tumor island but LH exhibits lower intensity staining (less hypoxia) compared to HH (greater hypoxia). At present, the discrimination of LH and HH is subjective but potentially the relative proportions of these populations may give useful clinical information. FIGURE 3B shows the resulting KNN classification after drawing four different small regions on the full histologic image. The grey-level coding for each biological structure is shown next to the classified image. Notice that all the structures of interest are identified rigorously, including the weakly stained blood vessels at the centre and upper-left corner. Some BG pixels that have been misclassified as LH are located close to the hypoxic regions touching the bottom border. These can be removed easily with the *remove_small_regions* routine (see CORRECTING MISCLASSIFICATIONS).

FIGURE 4A shows another example of a tissue section containing the structures of interest, but this time with low staining intensity. Small areas, indicated by arrows, in the BG and close to the LH regions have been mistaken as BV resulting misclassifications in the labeled image (FIG. 4B). For this image the routines included in the *correcting_misclassifications* module (see FIG. 1) were applied to remove those mislabeled pixels. FIGURE 4A also shows the final output image containing the borders of blood vessels and low hypoxic regions as well as the shortest line that connects each blood vessel with the closest hypoxic region. This is a routine included in the *perform_measurements* section of the software tool developed,[19] where a variety of other quantitative measurements can be performed (e.g., vascular density, blood vessel shape analysis, and LH to HH fraction). These measures will be tested in clinical specimens to establish whether they can provide potential prognostic information or can be used to assess the changes after radio- or chemotherapy.

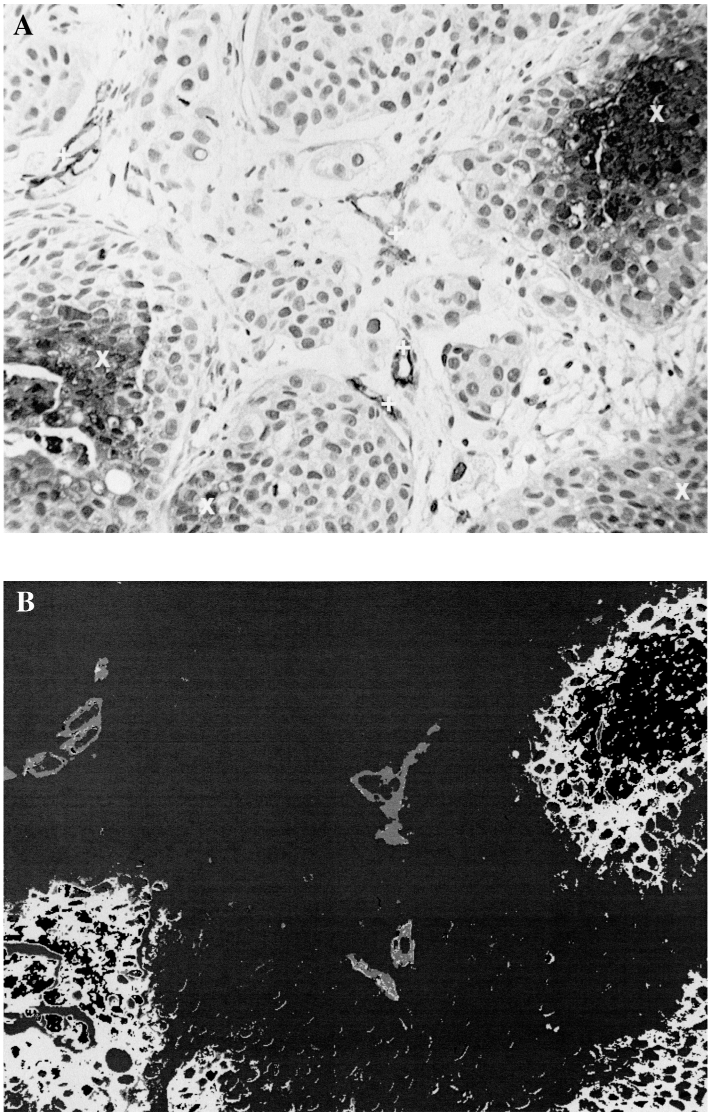

FIGURE 3. **(A)** A tissue section image with good staining quality: + denotes a blood vessel and × a hypoxic region. **(B)** The output image after pixel classification. ■, HH; ░, LH; ▒, BV; ▓, BG.

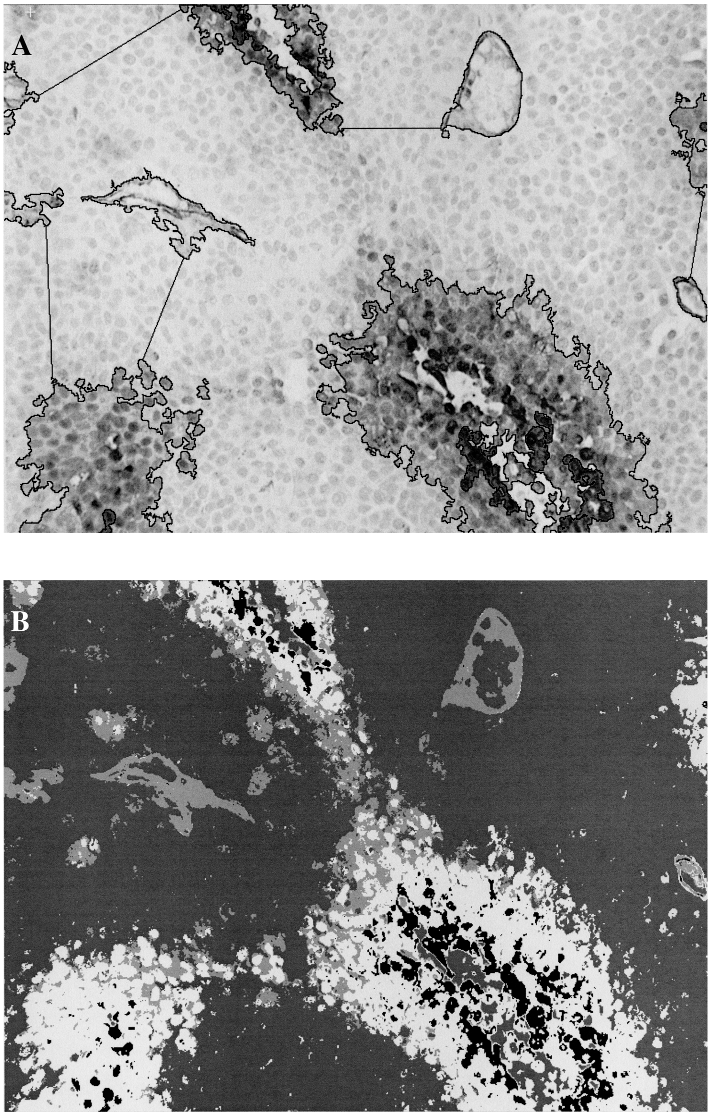

FIGURE 4. **(A)** A tissue section image with low staining quality and the borders of the hypoxic regions with their minimum distances to the nearest blood vessel, as found by the system. **(B)** The output image after pixel classification.

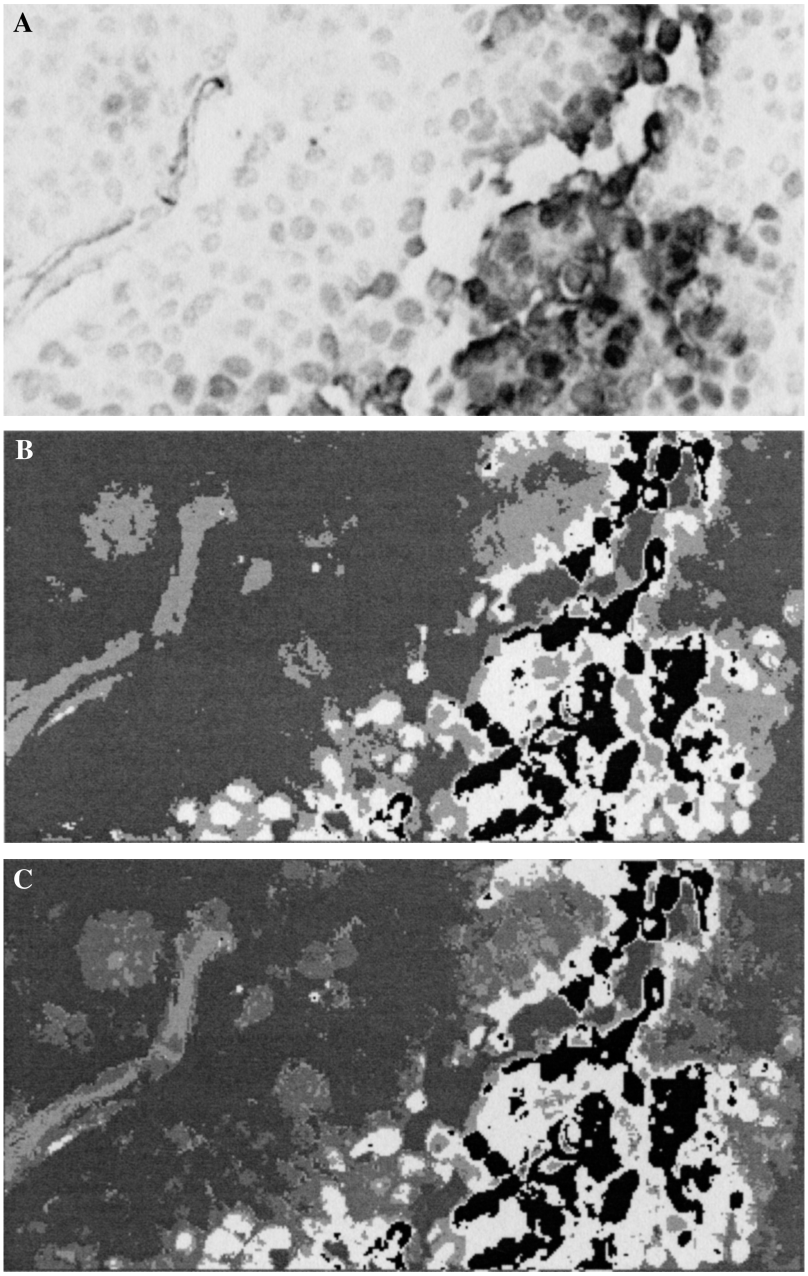

FIGURE 5. (A) Image portion from a tissue section showing typical BG and LH regions having false uptake of the vessel stain. **(B)** The output image using four classes. **(C)** Correct identification of falsely stained areas (*light gray*) and the blood vessel (*dark gray*), using five classes instead.

In conclusion, the algorithm was tested on a series of histologic images with very encouraging results (overall sensitivity between 82% and 95% and overall specificity between 93% and 99%), suggesting the high reliability of the proposed technique. We also studied the performance of the maximum likelihood classifier as a parametric technique (results are not shown), and the influence of adding more (RGBMrMgMb), or using different color features (L*a*b* and Lu*v*) during classification, but these failed to provide robust classifications. Furthermore, we have created a task-oriented image system that is very flexible and essentially parameter-free, providing the opportunity to perform quantitative measurements that are currently made manually and subjectively.

In addition, provision has been made for histologic images that exhibit very low staining quality, where the standard option is unable to remove mislabeled pixels after KNN classification, allowing the user to include one more class in order to model those regions having a color similar to that of other biological structures. A typical example is shown in FIGURE 5A. This is a small portion of a histologic image in which some BG nuclei have non-specific uptake of the vessel stain. Using four classes, the KNN classifier results in wrong classification of some BG regions as BV (FIG. 5B). However, the erroneously stained regions are detected robustly by increasing the number of classes to five, where the additional class corresponds to the BG areas having a color similar to that of blood vessels (FIG. 5C). Finally, if the hypoxic areas need to be partitioned into more than two regions, the user can select as many classes as required by drawing corresponding regions to the structures being modeled, and then proceed to the classification procedure.

ACKNOWLEDGMENTS

The financial support of the Cancer Research Campaign is gratefully acknowledged (CRC Grant SP 219510202). C. Loukas is funded by a postgraduate scholarship from the Cancer Research Campaign. We thank Mrs. R.J. Locke for development of the image acquisition software, Mr. R.G. Newman for assistance with hardware, Dr. A. Sibtain for providing the clinical specimens, and Mrs. F.M. Daley for the immunohistochemistry.

REFERENCES

1. SCHWARTZ, G. 1909. Uber desensibiliserung gegenrontgen und radiumstrahlen. Munchener Medizinischen Wochenschrift **24:** 1–2.
2. GRAY, L.H., *et al.* 1953. The concentration of oxygen dissolved in tissues at the time of irradiation as a factor in radiotrherapy. Br. J. Radiol. **26:** 638–648.
3. BROWN, J.M. 2000. Exploiting the hypoxic cancer cell: mechanisms and therapeutic strategies. Mol. Med. Today **6:** 157–161.
4. STONE, H.B., *et al.* 1993. Oxygen in human tumors: correlations between methods of measurement and response to therapy. Rad. Res. **136:** 422–434.
5. VAN DER SANDEN, B.P.J., *et al.* 1997. *In vivo* P-31 magnetic resonance spectroscopy and morphometric analysis of the perfused vascular architecture of human glioma xenografts in nude mice. Br. J. Cancer **75:** 432–1438.

6. PARLIAMENT, M.B., *et al.* 1992. Non-Invasive assessment of human tumor hypoxia with 123I-iodoazomycin arabinoside: preliminary report of a clinical study. Br. J. Cancer **65:** 90–95.
7. CHARPIN, C., *et al.* 1994. CD31 quantitative immunocytochemical assays in breast carcinomas. Anatom. Pathol. **103:** 443–448.
8. STRIETH, S., *et al.* 2000. Angiogenic switch occurs late in squamous cell carcinomas of human skin. Br. J. Cancer **82:** 591–600.
9. HAUSTERMANS, K., *et al.* 2000. Diffusion limited hypoxia astimated by vascular image analysis: comparison with pimonidazole staining in human tumours. Radiother. Oncol. **55:** 325–333.
10. RIJKEN, P.F.J., *et al.* 2000. Spatial relationship between hypoxia and the (perfused) vascular network in a human glioma xenograft: a quantitative multi-parameter analysis. Intl. J. Rad. Oncol. Biol. Phys. **48:** 571–582.
11. RIJKEN, P.F., H.J. BERNSEN & A.J. VAN DER KOGEL. 1995. Application of an image analysis system to the quantitation of tumour perfusion and vascularity in human glioma xenografts. Microvasc. Res. **50:** 141–153.
12. WYFFELS, K., *et al.* 2000. Vascular architecture and hypoxic profiles in human head and neck squamus cell carcinomas. Br. J. Cancer **83:** 674–683.
13. CHENG, H.D., *et al.* 2001. color image segmentation: advances and prospects. Pattern Recog. **34:** 2259–2281.
14. DUDA, R.O. & P.E. HART. 1973. Pattern Classification and Scene Analysis. J. Wiley & Sons, Inc., New York.
15. BISHOP, C.M. 1998. Neural Networks for Pattern Recognition. Oxford University Press, New York.
16. DUBUISSON-JOLLY M.-P. & A. GUPTA. 2000. Color and texture fusion: application to aerial image segmentation and GIS updating. Image Vision Comput. **18:** 823–832.
17. CHUANG, K.H. 1999. Model-free functional MRI analysis using Kohonen clustering neural network and fuzzy c-means. IEEE Trans. Med. Imag. Graphics **18:** 1117–1128.
18. LOUKAS, C.G., *et al.* 2000. An edge detection based approach for automated counting of cancer cell-nuclei in large-scale histological images. Proc. Med. Image Understand. Anal. 149–152.
19. LOUKAS, C.G. 2002. Quantitative Image Analysis of Biological Factors Influencing Radiotherapy. Ph.D. Thesis. University College London (UCL), London.